ADVANCED FUNCTIONAL MATERIALS
www.afm-journal.de

Reversible Polarity Control in 2D $MoTe_2$ Field-Effect Transistors for Complementary Logic Gate Applications

Byoung-Soo Yu, Wonsik Kim, Jisu Jang, Je-Jun Lee, Jung Pyo Hong, Namhee Kwon, Seunghwan Kim, Aelim Ha, Hong-Kyu Kim, Jae-Pyoung Ahn, Kwangsik Jeong, Takashi Taniguchi, Kenji Watanabe, Gunuk Wang, Jongtae Ahn, Soohyung Park,* and Do Kyung Hwang**

Precise control over polarity in field-effect transistors (FETs) plays a pivotal role in the design and construction of complementary metal–oxide–semiconductor (CMOS) logic circuits. In particular, achieving such precise polarity control in 2D semiconductors is crucial for the further development of advanced electronic applications beyond unit devices. This paper presents a systematic investigation on the reversible transition of carrier types in a 2D $MoTe_2$ semiconductor under different annealing atmospheres. Photoemission spectroscopy and density functional theory (DFT) calculations demonstrate that annealing processes in vacuum and in ambient air induce a modification in the density of states, resulting in alterations in *p*-type or *n*-type characteristics. These reversible changes are attributed to the physisorption and elimination of oxygen on the surface of $MoTe_2$. Furthermore, it is found that the device geometry affects the polarity of the transistor. By strategically manipulating both the annealing conditions and the geometric configuration, the *n*- and *p*-type unipolar characteristics of $MoTe_2$ FETs are successfully modulated and ultimately demonstrating that the functionality of not only a complementary inverter with a high voltage gain of ≈20, but also more complex logic circuits of NAND and NOR gates.

1. Introduction

Precise control over the polarity of charge carriers in semiconductors is crucial for constructing modern electronic circuit systems.[1–3] The conventional silicon semiconductor has been widely employed in various everyday electronic applications due to its capability to easily modulate the carrier type (*n*- or *p*-type) through ion implantation doping technology. 2D semiconductors have gained considerable attention as an emerging and significant class of materials, owing to their fascinating properties.[4,5] 2D materials not only offer opportunities for fundamental studies but also possess tremendous potential for advancing nanoelectronic and nanophotonic technologies.[3,4,6–8] Despite their merits, modulation of the polarities of 2D semiconductors remains a significant challenge. This obstacle could impede the further development of more advanced device

B.-S. Yu, J. Jang, J.-J. Lee, J. P. Hong, D. K. Hwang
Center for Opto-Electronic Materials and Devices
Post-Silicon Semiconductor Institute
Korea Institute of Science and Technology (KIST)
Seoul 02792, Republic of Korea
E-mail: dkhwang@kist.re.kr

B.-S. Yu, J.-P. Ahn, S. Park, D. K. Hwang
Division of Nanoscience & Technology
KIST School
University of Science and Technology (UST)
Seoul 02792, Republic of Korea
E-mail: soohyung.park@kist.re.kr

The ORCID identification number(s) for the author(s) of this article can be found under https://doi.org/10.1002/adfm.202404129

DOI: 10.1002/adfm.202404129

W. Kim, N. Kwon, S. Kim, A. Ha, H.-K. Kim, J.-P. Ahn, S. Park
Advanced Analysis and Data Center
Korea Institute of Science and Technology (KIST)
Seoul 02792, Republic of Korea

J. P. Hong, G. Wang, D. K. Hwang
KU-KIST Graduate School of Converging Science and Technology
Korea University
Seoul 02841, Republic of Korea

K. Jeong
Division of AI Semiconductor Science
Yonsei University
Wonju 26493, Republic of Korea

T. Taniguchi, K. Watanabe
Advanced Materials Laboratory
National Institute for Materials Science
Tsukuba 305-0044, Japan

J. Ahn
Department of Physics
Changwon National University
Changwon 51139, Republic of Korea
E-mail: jongtae@changwon.ac.kr

applications, such as homogeneous complementary metal–oxide–semiconductor (CMOS) circuits.[1,9] Considerable effort has been devoted to controlling the polarities of 2D transistors, leading to various doping strategies such as solid-state diffusion,[10] charge transfer doping,[11] and substitutional doping.[12] However, these methods often involve complicated fabrication processes and may result in physical and/or chemical damage, such as surface contamination and the creation of structural defects.[13,14] Recently, several studies have highlighted the fundamental role of Schottky barriers at the metal–2D semiconductor junction in determining the carrier type of 2D transistors.[9,15–17] Schottky barrier engineering allows for the simultaneous injection of both electrons and holes into the 2D semiconductor, offering precise control over its polarity.[18,19] But one challenging issue remains to be resolved: Fermi level pinning.[2,20–22] Moreover, while the aforementioned approaches facilitate polarity transitions from *n*-type to *p*-type or vice versa,[5,23–25] an investigation into reversible transitions has not been systematically conducted to date.

In the meantime, device geometry could be a critical factor in determining the polarity of a 2D transistor because the gate field plays a key role in controlling the flow of charge carriers and influencing their behavior in the 2D active channel.[26] Even under the same doping conditions, the aspects of polarity transitions can exhibit variation due to the influence of the gate field and other structural factors. The interplay between device geometry (i.e., gate field distribution) and intrinsic property changes of a 2D semiconductor therefore contributes to the complex behavior of charge carriers within a 2D transistor. Despite this fact, a systematic investigation into the correlation among intrinsic property changes, device geometry effects, and the resulting polarity of a 2D transistor is still lacking.

Here, we present a demonstration of a reversible polarity transition between unipolar *n*- and *p*-type characteristics of a molybdenum ditelluride ($MoTe_2$) semiconductor, which is achieved through facile annealing processes under controlled environments: air and vacuum conditions. This reversible polarity transition in the $MoTe_2$ layer can be correlated with oxygen physisorption and desorption during air annealing and vacuum annealing, respectively, with supporting evidence from photoemission spectroscopy results and density functional theory (DFT) calculations. In addition, it is found that the gate electric field at the $MoTe_2$/contact electrode interface has a significant impact on the polarity of the transistor. By combining optimized annealing conditions with appropriate device geometries in the design and fabrication stages, $MoTe_2$ field-effect transistors (FETs) exhibit reversible unipolar *n*- and *p*-type characteristics. Based on this finding, we have successfully implemented a homogeneous complementary logic inverter consisting of symmetric unipolar *n*- and *p*-type $MoTe_2$ FETs, which achieved a high gain value of ≈20 at V_{DD} = 5 V. In addition, this is also extended to construct more complex logic gate applications such as NAND and NOR. The proposed polarity control technique strengthens the potential of 2D electronic devices in high-performance functional applications.

2. Results and Discussion

In order to understand the influence of air on the density of states (DOS) of $MoTe_2$, a series of ultraviolet photoelectron spectroscopy (UPS) and X-ray photoelectron spectroscopy (XPS) measurements were conducted in a step-by-step manner. First, 2H-$MoTe_2$ crystals were prepared by mechanical exfoliation under ultrahigh vacuum conditions of 10^{-9} torr, enabling the measurement of the intrinsic DOS of $MoTe_2$. Subsequently, the $MoTe_2$ samples underwent three annealing steps, each consisting of 90 min of annealing in air, 90 min of annealing under vacuum, and 30 min of annealing in air. **Figure 1a–e** shows representative UPS and XPS spectra of $MoTe_2$ obtained at various annealing steps conducted in a sequential order: as-exfoliated (black line), air annealing for 90 min (blue line), vacuum annealing for 90 min (red line), and subsequent air annealing for 30 min (light blue line). Figure 1a,b displays the UPS spectra in the secondary cutoff (SECO) and valence band regions, respectively, indicating the work function (WF) and the frontier orbital of $MoTe_2$. The bottommost line (black) shows that the WF of the exfoliated $MoTe_2$ flake was measured to be 4.25 eV. The valence spectral features of the $MoTe_2$ flake in Figure 1b show its intrinsic DOS, having a valence band maximum (VBM) of 0.77 eV obtained from the onset of the spectrum. Based on the reported optical bandgap of ≈1.0 eV,[25,27,28] the conduction band minimum (CBM) of the exfoliated $MoTe_2$ flake can be estimated to be 0.23 eV. This finding reveals that the exfoliated $MoTe_2$ flake exhibits a strong *n*-type characteristic. It can be explained that, in general, $MoTe_2$ contains intrinsic Te vacancy defect sites due to their low formation energy,[29] which generate new energy states close to the conduction band edge.[30] This can induce *n*-type conduction in $MoTe_2$ by leaving behind electrons ($V_{Te}^{\bullet\bullet} + 2e^- = Te_2$).[31,32] As a result, $MoTe_2$ may be highly sensitive to the adsorption of O_2 or H_2O molecules that are abundant in ambient atmosphere.[23,33]

After annealing in ambient conditions (blue lines), new peaks emerge in the XPS spectra of Te 3d, Mo 3d, and O 1s (Figure 1c–e, respectively), providing direct evidence of oxidation. Simultaneously, the WF of the $MoTe_2$ flake increased to 4.89 eV, while the valence band features broadened with a shift in onset to 0.37 eV. This suggests that surface oxidation changes the carrier type of $MoTe_2$ from strong *n*-type to *p*-type. Next, we performed vacuum annealing to remove the adsorbed O_2 or H_2O molecules, which was mostly successful as shown with the red lines in Figure 1a–e. A comparison of the UPS spectra (Figure 1a,b) obtained from as-exfoliated and vacuum-annealed samples reveals that, except for a very slight spectrum broadening, the spectra are nearly identical. Upon closer inspection of the Mo 3d spectra, the Mo—O interaction (yellow peak) is observed to be partially irreversible even after vacuum annealing. It becomes apparent that while the dominant contribution is from reversible oxidation, only a very small contribution from irreversible oxidation occurs simultaneously. In contrast, the Te 3d spectra shows fully reversible oxidation/deoxidation behaviors. The changes observed in the O 1s core level spectra (Figure 1e) support above two contributions of oxidation/deoxidation processes.

Additionally, we conducted identical experiments in controlled environments with H_2O and O_2 to determine the relative significance of each and to elucidate their respective roles based on the observed phenomena described above. For this, deionized (DI) water was drop-casted onto the clean surface of $MoTe_2$, while annealing itself was carried out in a pure O_2 atmosphere (99.99%,

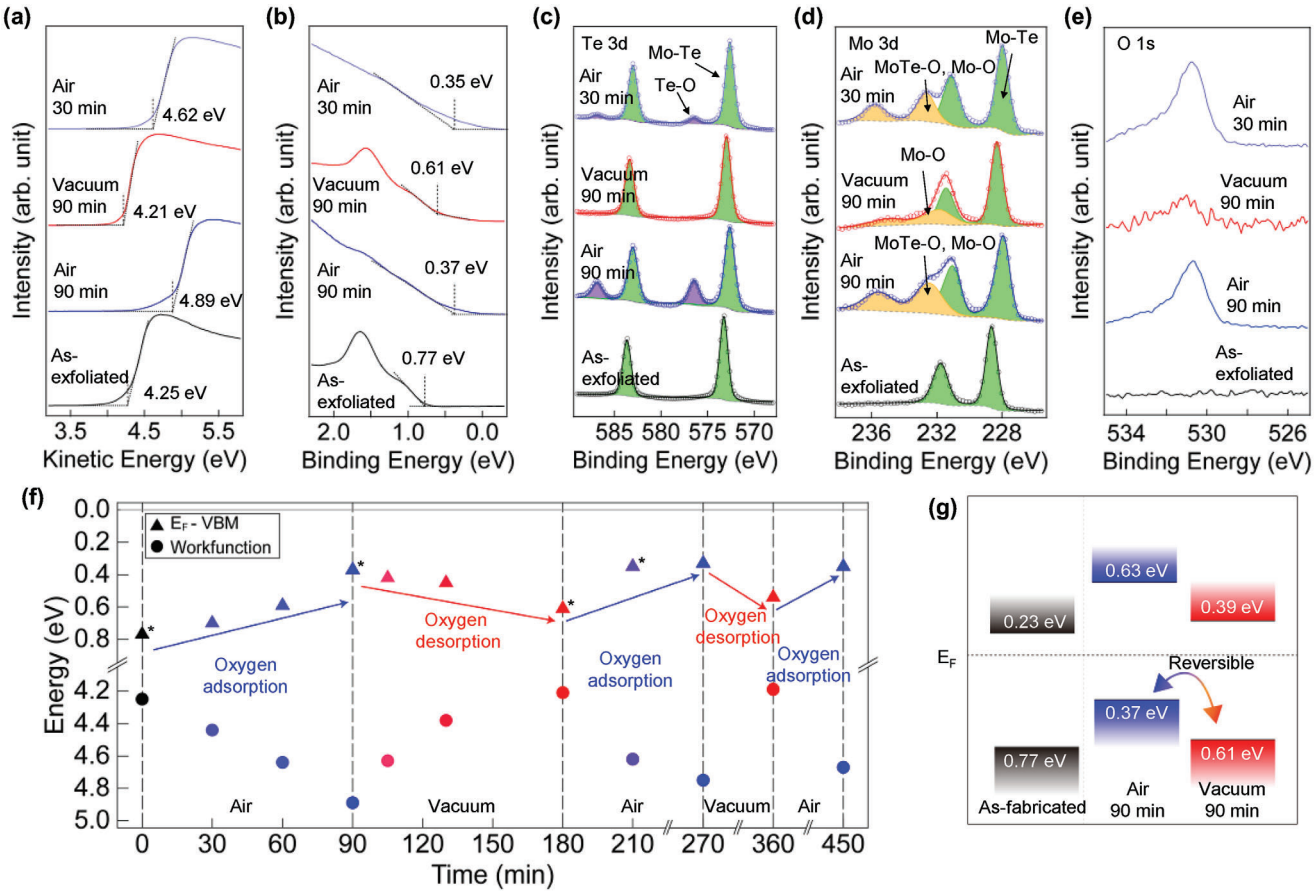

Figure 1. Representative a) secondary cutoff and b) valence region UPS and XPS spectra of c) Te 3d, d) Mo 3d, and e) O 1s of $MoTe_2$ obtained at various annealing steps conducted in the following sequential order: as-exfoliated (black line), air annealing for 90 min (blue line), vacuum annealing for 90 min (red line), and subsequent air annealing for 30 min (light blue line). f) Summarized work function and valence band maximum as a function of the repeated air and vacuum annealing steps. g) Energy level of $MoTe_2$ as-exfoliated (black), 90 min air annealing (blue), and 90 min vacuum annealing (red).

1 atm). As depicted in the UPS spectra (Figure S1a,b, Supporting Information), annealing in an O_2 atmosphere resulted in a pronounced polarity shift from *n*-type to *p*-type, closely resembling the changes observed with air annealing. However, H_2O had negligible influence on the polarity of $MoTe_2$, indicating that H_2O molecules are not the predominant factors contributing to the oxidation observed previously. Similarly, XPS spectra obtained from samples annealed in an O_2 atmosphere clearly revealed evidence of oxidation, whereas no such evidence was identified following drop-casting of DI water (Figure S2a–c, Supporting Information). Therefore, we can conclude that O_2 molecules are the primary factors responsible for the oxidation process on the surface of $MoTe_2$.

From the spectral information, we can establish the following hypothesis regarding surface oxidation. O_2 molecules tend to easily dissociate into two oxygen atoms after adsorption on top of the $MoTe_2$ layer.[34] Afterward, the oxygen atoms can either be located 1) on the top of chalcogen Te atoms or 2) in Te vacancy sites (or edges), leading to the formation of Mo—O bonds in the $MoTe_2$ structure.[23,29,35] The atomic configuration of these two oxygen atom locations is discussed in more detail below using DFT calculations.

Figure 1f summarizes the WF and VBM as a function of repeated air and vacuum annealing steps as measured in the following manner. When $MoTe_2$ flake is annealed in air, the VBM gradually shifts toward the Fermi energy (E_F) and the WF increases over the annealing time. However, when annealed in vacuum, the opposite trend is observed. In short, annealing in air and vacuum can reversibly control the polarity transition, i.e., change in the carrier type of $MoTe_2$ between *n*- and *p*-type, except for the small contribution of Mo—O interaction. The energy levels of $MoTe_2$ measured during air and vacuum annealing are plotted in Figure 1g.

We then performed DFT calculations to confirm the polarity transition through oxygen adsorption/desorption and investigate the impact of the atomic structure of two distinct oxygen adsorptions (on the top of chalcogen Te atoms and in Te vacancy sites) on the changes in the electronic structure of the $MoTe_2$ layer, as suggested by the XPS spectra. **Figure** 2a,b depicts the energy band structure and atomic structure of $MoTe_2$ with and without a Te vacancy, which are well-matched with the previously reported band structure.[29,30,36] In Figure 2b, we observe weak localized states (red) induced by a Te vacancy near the CBM. These states can act as electron donor states, leading to *n*-type properties. From this

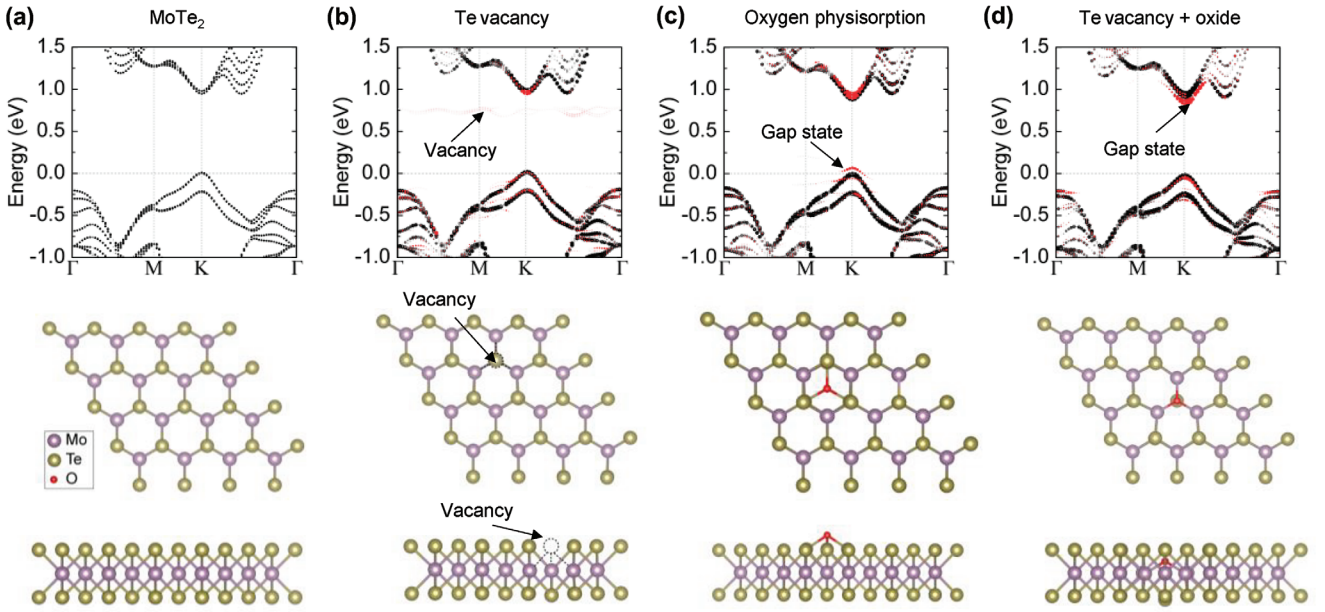

Figure 2. Calculated electronic band structure along with top and side views of the atomic structure for a) intrinsic $MoTe_2$, b) Te-defective $MoTe_2$, c) $MoTe_2$ with oxygen physisorption, and d) oxygen-incorporated Te-defective $MoTe_2$. Red dashed lines represent defects, oxygen physisorption, or oxygen-incorporated Te-defective states in the electronic band structures.

finding, we can explain the *n*-type characteristics observed in the UPS measurement results of pristine $MoTe_2$ by the presence of naturally occurring defects in pristine $MoTe_2$.

Upon oxygen adsorption, localized states induced by oxygen components appear within the bandgap in both cases, as shown in red in Figure 2c,d. First, in the case of $MoTe_2$ without Te defects, the bottom of Figure 2c illustrates the most stable atomic position of oxygen, corresponding to physisorption. In this case, the gap state is very close to the VBM, and it therefore operates as an electron acceptor state, leading to $MoTe_2$ exhibiting *p*-type characteristics. In contrast, when oxygen is in a Te vacancy site, the electronic structure (band structure and bandgap) undergoes significant changes due to strong Mo—O chemical bonding, and this is accompanied by the appearance of oxygen-induced states near the CBM (red). This barely induces *p*-type characteristics, unlike the physisorption of oxygen on top of defect-free $MoTe_2$. In summary, in pristine $MoTe_2$, the physisorption and desorption of oxygen are reversible processes, resulting in a reversible shift between *n*- and *p*-type characteristics. On the other hand, when oxygen is located in a defect site, its lower probability of being thermally separated leads to irreversible changes in the electronic structure of $MoTe_2$.

One of the most efficient methods to examine phase changes in 2D materials is Raman spectroscopy. Here, the Raman spectrum of as-exfoliated 2H-$MoTe_2$ flake indicates three obvious peaks corresponding to the out-of-plane A_{1g} mode, in-plane E^1_{2g} mode, and bulk in-active B^1_{2g} mode, at 173, 233, and 289 cm^{-1}, respectively (Figure S3a, Supporting Information). The observed peaks in the $MoTe_2$ flakes remain practically unchanged after air annealing, indicating that the original semiconducting 2H phase in the bottom layers is entirely maintained without structural damage or major compositional changes in the $MoTe_2$ layer.[37] Furthermore, the Raman peak of h-BN in the vertically stacked h-BN/$MoTe_2$ structure remained unshifted upon air annealing, indicating that the interfacial properties were not chemically altered by oxygen adsorption (Figure S3b, Supporting Information). This result supports that the carrier type of $MoTe_2$ can be reversibly controlled by repetitive annealing processes, as shown in the UPS and XPS analysis of Figure 1.

After conducting fundamental characterizations using the above-mentioned photoemission spectroscopy and theoretical calculations, $MoTe_2$ FETs were fabricated to examine the possibility of reversible polarity transitions in actual devices. At first, we used the conventional bottom-gate top-contact geometry, in which a gate electrode is overlapped with source/drain (S/D) contact electrodes as depicted in **Figure 3**a,b. The thicknesses of the $MoTe_2$ channel and h-BN dielectric were measured to be ≈16 and 10 nm, respectively, from the atomic force microscopy (AFM) profile (Figure S4a,b, Supporting Information). Figure 3c displays the transfer characteristics of the $MoTe_2$ FET as-fabricated, after vacuum annealing, and after air annealing; the output characteristics are shown in Figure S4c,d (Supporting Information). Interestingly, the as-fabricated $MoTe_2$ FET exhibited *p*-type behavior, in contrast to the *n*-type behavior observed in the as-exfoliated $MoTe_2$ used for spectroscopic analysis in Figure 1. This *p*-type conduction can be attributed to the adsorption of oxygen atoms during device fabrication under an air atmosphere. The as-fabricated device is consistent with the results of the air annealing steps in the spectroscopy analysis. It is worth noting that ambipolar behaviors were observed after further vacuum annealing and air annealing, rather than unipolar carrier-type transitions. After vacuum annealing, n-dominant ambipolar behavior was observed, where the electron current was one order of magnitude higher than the hole current. On the other hand, a p-dominant ambipolar behavior was achieved after air annealing, with the hole current dominating over the electron current. We

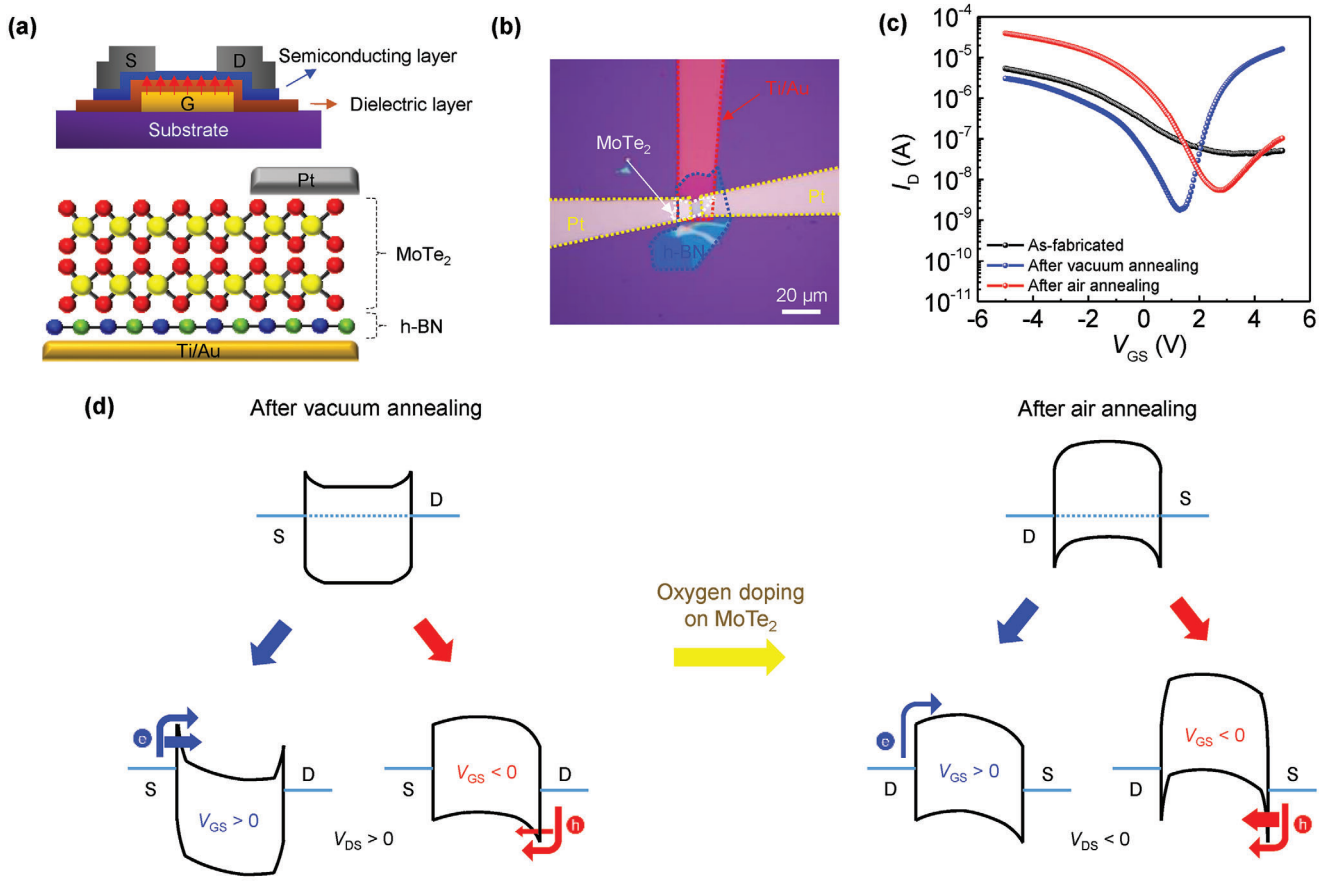

Figure 3. a) Conventional bottom-gate top-contact device geometry and schematic illustration of the atomic structure around the $MoTe_2$/Pt contact area. b) Optical microscopy image of the $MoTe_2$ FET. c) Transfer characteristics of the $MoTe_2$ FET as-fabricated (drain bias, $V_{DS} = -1$ V), after vacuum annealing ($V_{DS} = 1$ V), and after air annealing ($V_{DS} = -1$ V). d) Energy band diagrams of the $MoTe_2$/Pt contact at equilibrium and under positive and negative V_{GS}.

hypothesize that charge injection from the $MoTe_2$/Pt contact, modulated by gate bias (V_{GS}), is correlated with the observed ambipolar behaviors. Figure 3d exhibits energy band diagrams of the $MoTe_2$/Pt contact at equilibrium and under positive and negative V_{GS}. Considering the Fermi level pinning effect observed in previously reported research, the energy level of the Pt electrode is determined to be slightly above the midgap level of $MoTe_2$.[38] After vacuum annealing (*n*-type $MoTe_2$), the contact pinning resulted in a small downward band bending at equilibrium. When a positive V_{GS} (gate–source voltage) is applied, the downward band bending allows electrons to undergo both thermionic emission and tunneling, which, in turn, contribute to a high electron current of 1.63×10^{-5} A at $V_{GS} = +5$ V. On the other hand, the upward band bending caused by a negative V_{GS} hinders electron injection but allows for the possibility of hole conduction. Due to a larger barrier width, a relatively lower but still considerable hole current of 3.08×10^{-6} A at -5 V was observed. After air annealing, an opposite trend becomes apparent. The p-doping effect leads to upward band bending in the equilibrium state. Under positive V_{GS}, only weak electron injection is observed because of the large barrier. In contrast, the large upward bending by negative V_{GS} facilitates hole injection, resulting in a high hole current of 3.96×10^{-5} A at -5 V. In order to confirm reproducibility, five more batches with the same geometry were fabricated and examined for individual device characteristics (Figure S5a–c, Supporting Information). Similar n-dominant and p-dominant ambipolar characteristics were observed with current ratios (I_{5V}/I_{-5V}) of $\approx 5 \times 10^0$ and 4×10^{-2} after vacuum annealing and air annealing, respectively. These results indicate that a proper device geometry is essential to achieve polarity transitions for unipolar electron or hole conduction.

After observing the results with the conventional geometry, we now propose utilizing a locally aligned bottom-gate top-contact geometry, wherein the gate electrode does not overlap with the S/D contact electrodes as depicted in **Figure** 4a,b. In this configuration, V_{GS} specifically influences the semiconducting layer that is in contact with the gate electrode, and consequently, the intrinsic regions of $MoTe_2$ near the S/D contact, unaffected by V_{GS} modulation, would play a crucial role in the polarity transition. The line width of the locally aligned bottom-gate was measured to be ≈ 6 μm (Figure 4b), and the thicknesses of the $MoTe_2$ channel and h-BN dielectric were estimated to be ≈ 18 and 10 nm, respectively (Figure S6a,b, Supporting Information). Figure 4c plots the transfer characteristics of the $MoTe_2$ FET with locally aligned bottom-gate top-contact geometry as-fabricated, after vacuum annealing, and after air annealing. The output characteristics

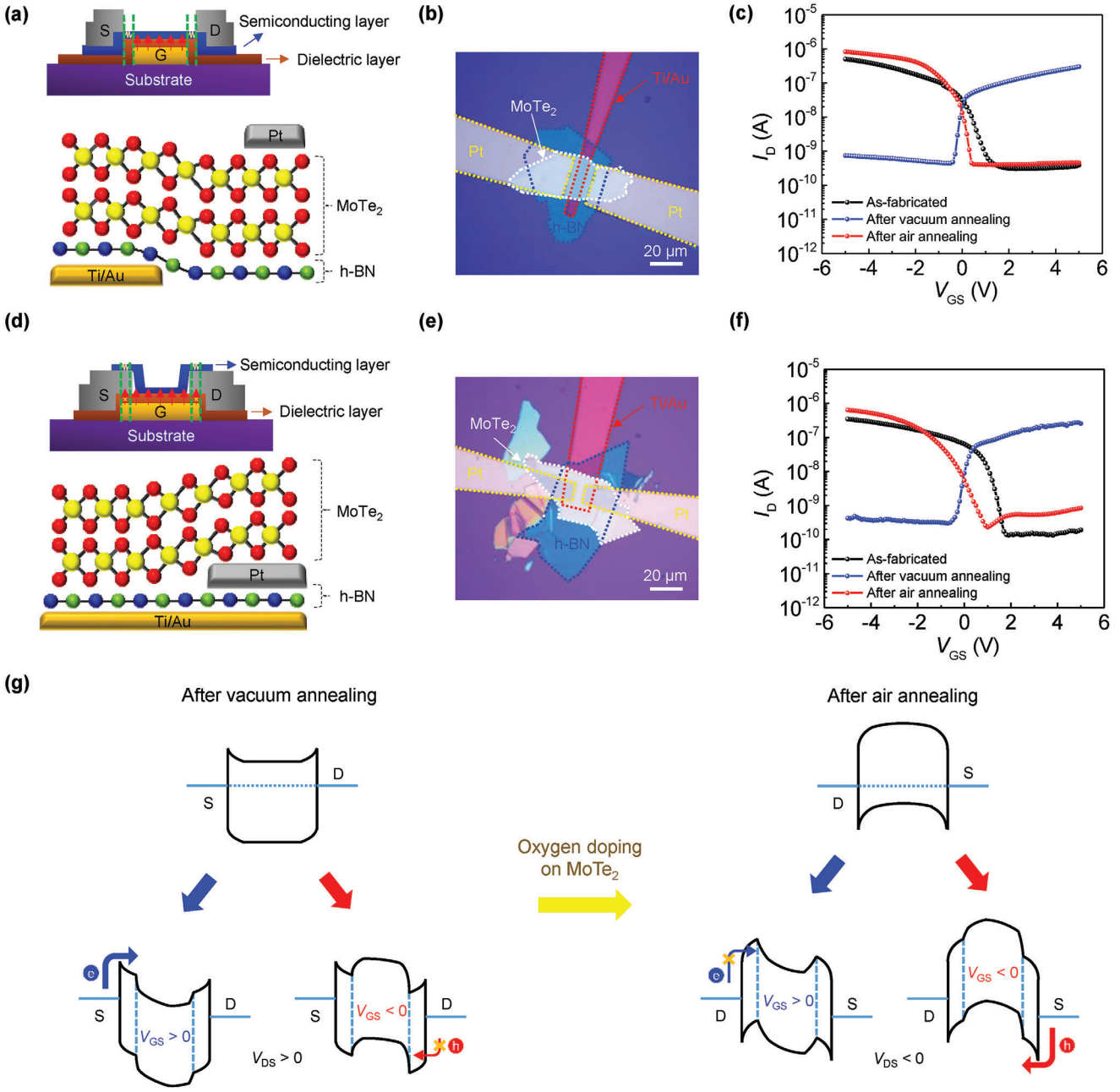

Figure 4. a) Locally aligned bottom-gate top-contact and d) bottom-gate bottom-contact device geometries and corresponding schematic illustrations of the atomic structure around the $MoTe_2$/Pt contact area. b,e) Optical microscopy images of the $MoTe_2$ FETs in (a) and (d). Transfer characteristics of c) locally aligned bottom-gate top-contact and f) bottom-gate bottom-contact $MoTe_2$ FETs as-fabricated ($V_{DS} = -1$ V), after vacuum annealing ($V_{DS} = 1$ V), and after air annealing ($V_{DS} = -1$ V). g) Energy band diagrams of the $MoTe_2$/Pt contact at equilibrium and under positive and negative V_{GS}.

are shown in Figure S6c,d (Supporting Information). As expected, the as-fabricated device showed *p*-type behavior and a reduced off current on the order of 10^{-10} A due to the presence of relatively high-resistance intrinsic regions. More importantly, unlike the previous conventional bottom-gate top-contact device, the $MoTe_2$ FET with locally aligned bottom-gate top-contact geometry clearly exhibited reversible unipolar transitions from *p*-type to *n*-type through vacuum annealing and from *n*-type to *p*-type through air annealing. Five more device batches were also investigated (Figure S7a–c, Supporting Information), and clear polarity transitions between unipolar *n*- and *p*-type conduction (I_{5V}/I_{-5V}: $\approx 1 \times 10^3$ in vacuum annealing and 5×10^{-4} in air annealing) were achieved. An alternative device architecture that could also lead to a similar polarity transition is bottom-gate bottom-contact geometry, in which case the $MoTe_2$ regions in the contact areas are barely affected by V_{GS} due to the S/D electrodes, resulting in these edges acting as intrinsic regions. Figure 4d,e shows a cross-sectional view and optical microscope image of

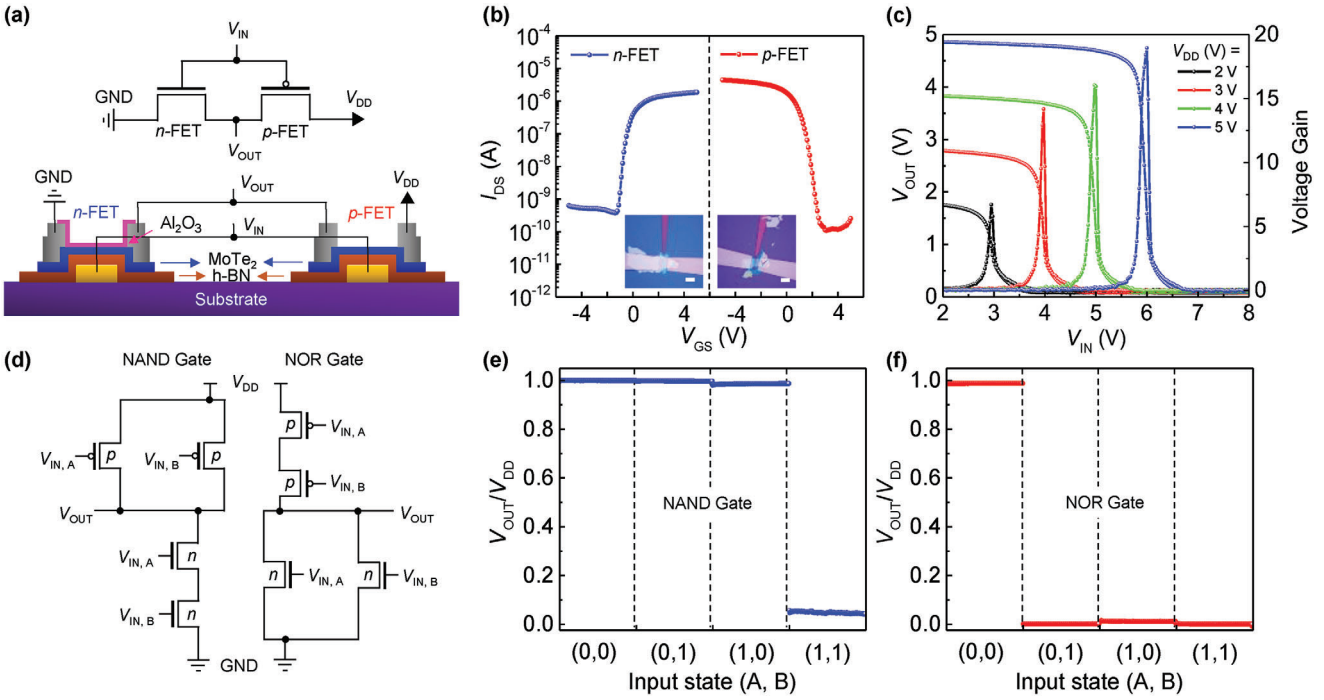

Figure 5. a) Cross-sectional view of the complementary inverter circuit design composed of *n*- and *p*-type $MoTe_2$ FETs with locally aligned bottom-gate top-contact geometry. The n-FET and p-FET were obtained by vacuum annealing and air annealing, respectively. b) Transfer characteristics and optical microscopy images (insets, scale bar 20 µm) of the n-FET with Al_2O_3 passivation film and the p-FET. c) Output voltage (left axis) and voltage gain (right axis) of the inverter as a function of V_{DD} from 2 to 5 V with a step of 1 V. d) Circuit diagrams of NAND and NOR gates consisting of four $MoTe_2$ FETs (two *p*-type transistors and two *n*-type transistors). Output voltages of e) NAND and f) NOR gates as a function of input states ($V_{IN\,A}$, $V_{IN\,B}$) at V_{DD} = 4 V. A V_{IN} of 0 and 8 V was used as input '0' and '1', respectively.

a $MoTe_2$ FET with bottom-gate bottom-contact geometry. Multilayer $MoTe_2$ with a thickness of ≈26 nm and h-BN dielectric of ≈16 nm were used (Figure S8a,b, with output characteristics shown in Figure S8c,d, Supporting Information). Based on the transfer characteristics (Figure 4f), consistent behaviors were clearly observed in the following order: initial *p*-type behavior during fabrication, *n*-type transition during vacuum annealing, and *p*-type transition during air annealing. Five additional batches also showed clear majority carrier types as electrons (vacuum annealing) and holes (air annealing), with $I_{5V}/I_{-5\,V}$ ratios of ≈9×10^2 and 1×10^{-3}, respectively (Figure S9a–c, Supporting Information).

These consistent results obtained from $MoTe_2$ FETs with both locally aligned bottom-gate top-contact and bottom-gate bottom-contact geometries confirm that the intrinsic regions unmodulated by V_{GS} are a critical factor in determining the polarity transition. The energy band diagrams of the $MoTe_2$/Pt contact, as depicted in Figure 4g, explain the underlying physical mechanism. In the equilibrium state, the band alignments are similar to those in the conventional bottom-gate top-contact device. However, the intrinsic regions of $MoTe_2$ near the metal–semiconductor junction retain their initial band structure despite the applied V_{GS}. In the case of vacuum-annealed devices, electrons can be injected and transported under positive V_{GS}, while hole injection cannot occur under negative V_{GS} due to the high barrier height and width induced by the intrinsic region. As a result, unipolar *n*-type characteristics were clearly observed in the transfer curves (Figure 4c,f). On the other hand, after air annealing, only hole conduction is possible under negative V_{GS}, resulting in unipolar *p*-type characteristics.

Furthermore, we also investigated the key molecules that induce oxidation and the *p*-type doping effect in actual $MoTe_2$ devices. In order to compare with that from air annealing, O_2 annealing was carried out after vacuum annealing using locally aligned bottom-gate top-contact geometry. The $MoTe_2$ FETs clearly presented the polarity transition from *n*-type to *p*-type through O_2 annealing, indicating that the O_2 atmosphere causes a nearly identical polarity change compared with air atmosphere (Figure S10a,b, Supporting Information). From these device characteristics, it was found that the *p*-type transition of $MoTe_2$ FETs can also be mainly attributed to O_2 molecules.

By combining the annealing conditions with the above device geometry (locally aligned bottom-gate top-contact), we now demonstrate a homogeneous CMOS logic gate application. First, an inverter circuit, the simplest logic gate, was constructed as shown in **Figure 5**a. In order to prevent *p*-type doping effects in the n-FET by adsorption of oxygen atoms onto the $MoTe_2$ layer before device measurement, a thin (10 nm) aluminum oxide (Al_2O_3) layer was deposited on the device as a passivation layer via atomic layer deposition (ALD). Figure 5b exhibits unipolar *n*- and *p*-type transfer characteristics. Interestingly, the on current of the n-FET increased by approximately one order of magnitude after the Al_2O_3 deposition compared to the vacuum-annealed device (Figure 4c), rising from the order of 10^{-7} to 10^{-6} A. This enhancement is due to the Al_2O_3 ALD process, which promotes n-type conduction.[23,39,40] Figure 5c displays the voltage transfer

characteristics and voltage gain curves of the homogeneous complementary inverter circuit at various supply voltages (V_{DD}). The inverter exhibits a distinct logic output with a sharp voltage transition, attaining a high gain of ≈20 at a V_{DD} of 5 V. Then for a more complex application, we constructed NAND and NOR logic circuits by integrating four $MoTe_2$ FETs, comprising two *p*-type transistors and two n-type transistors, as illustrated in the circuit diagram of Figure 5d. Optical images and transfer characteristics of the four transistors are respectively provided in Figure S11a,b (Supporting Information). As depicted in Figure 5e,f, the output voltages demonstrate that the $MoTe_2$ FETs facilitate the successful operation of NAND and NOR gates. The *p*-type doping effect under air exposure for more than one day weakened the n-type polarity (Figure S12, Supporting Information), indicating the necessity for further studies to achieve long-term stability of n-FETs. While efforts should be made to enhance the stability of n-type characteristics, our straightforward and efficient annealing strategy for *n*- or *p*-doping allows for precise control of the polarity in $MoTe_2$ devices, enabling the implementation of not only a high-performance homogeneous CMOS inverter but also more complex NAND and NOR logic gates.

3. Conclusion

We have controlled the polarity transition between unipolar *n*- and *p*-type characteristics of a $MoTe_2$ semiconductor through the use of air annealing and vacuum annealing. The reversible polarity transition in the $MoTe_2$ layer can be attributed to the adsorption and desorption of oxygen atoms during the annealing steps, as supported by photoemission spectroscopy results and DFT calculations. In addition, we identified the critical role played by the intrinsic regions of $MoTe_2$ near the S/D contact, which remained unmodulated by V_{GS}, in the polarity transition of the devices. By employing both locally aligned bottom-gate top-contact and bottom-gate bottom-contact geometries along with appropriate annealing conditions, we achieved reversible unipolar *n*- and *p*-type characteristics in $MoTe_2$ FETs. This achievement was further validated through the successful operation of a high-performance homogeneous CMOS logic inverter and more complex NAND and NOR logic gates leveraging unipolar *p*- and *n*-type $MoTe_2$ FETs. We believe that our proposed strategy provides an effective means for precise polarity control of 2D semiconductors, thus paving the way for the advancement of 2D nanoelectronics.

4. Experimental Section

Characterization of $MoTe_2$ Samples: XPS and UPS experiments were conducted using a PHI VersaProbe instrument to analyze the electronic structure of multilayer $MoTe_2$ flakes after each vacuum, air, and O_2 annealing. For XPS, a micro-focused and monochromatic Al Ka (1486.6 eV) discharging lamp was utilized as the excitation light source, while a He I (21.22 eV) discharging lamp was used for UPS. The energy references of both μ-XPS and UPS were calibrated with respect to the Fermi level of Au (111) single crystal. To ensure accurate measurements, a −15 V potential was applied to the samples to determine the reliable secondary electron cutoff. The thicknesses of the h-BN and $MoTe_2$ nanoflakes were measured with a Park Systems XE 100 AFM system. Additionally, Raman spectroscopy (LabRAM HR Evolution, Horiba Jovin Yvon) was performed with a laser excitation wavelength of 532 nm to investigate the scattering features of the $MoTe_2$ layers before and after air annealing.

Density Functional Theory (DFT): Model super cells of $MoTe_2$ used in this work were expanded to a large volume of 14.2 × 14.2 × 61.3 $Å^3$ (4 × 4, 4th monolayer) with a 30 Å vacuum slab. The projector augmented wave (PAW) method as implanted in the Vienna Ab initio Simulation Package (VASP) was used for calculations. Standard spin-polarized calculations (collinear) were performed. The electron wave functions were expanded up to an energy cutoff of 500 eV and Monkhorst-Pack 4 × 4 ×1 k-point sampling was used. To obtain the band structure of the supercell, band unfolding was performed based on the effective band structure (EBS) method.[41] The convergence criteria for structure optimization and energy calculation were set to accurate quality with SCF tolerance and an energy of 1.0 × 10^{-5} eV $atom^{-1}$. The calculated band structures were rigidly shifted to align with the Fermi level and valence band maximum of $MoTe_2$ to ensure a clear comparison.

Device Fabrication and Characterization: Ti (1 nm)/Au (10 nm) bottom gate electrodes were deposited on Si/SiO_2 substrate using direct current (DC) magnetron sputtering and patterned through the photolithographic liftoff process. The top- and bottom-contact devices had gate lengths of 20 μm, while the locally aligned bottom-gate top-contact device had a gate length of 6 μm. Subsequently, h-BN nanoflakes were used as gate dielectrics, mechanically exfoliated using a poly(dimethylsiloxane) stamp. They were then transferred onto the pre-deposited gate electrodes in the three different device geometries. For the bottom-gate top-contact devices, $MoTe_2$ nanoflakes were exfoliated and transferred onto the pre-deposited h-BN flakes. Pt (20 nm) was deposited using DC magnetron sputtering as S/D electrodes and patterned using photolithography. For the bottom-gate bottom-contact devices, the S/D electrodes were formed on the h-BN dielectric, and the $MoTe_2$ semiconducting layer was prepared using the above-mentioned method. All electrical measurements of the $MoTe_2$ FETs were performed using a semiconductor parameter analyzer (4200-SCS Keithley). Vacuum annealing of the $MoTe_2$ devices was conducted at 200 °C for 30 min in a vacuum chamber, followed by measurement in vacuum (≈10^{-2} torr) at room temperature. Air annealing of the $MoTe_2$ devices was conducted at 200 °C for 10 min on a hot plate, followed by measurement in ambient air at room temperature. The $MoTe_2$ devices underwent O_2 annealing at 200 °C for 10 min with a flow rate of 20 sccm, followed by measurement in ambient air at room temperature. The electrical characteristics of the homogenous $MoTe_2$ CMOS inverter and NAND/NOR gates were measured using a semiconductor parameter analyzer (Agilent 4156 B) in a dark shield box.

Supporting Information

Supporting Information is available from the Wiley Online Library or from the author.

Acknowledgements

B.-S.Y. and W.K. contributed equally to this work. D.K.H. and S.P. acknowledge financial support from the Korea Institute of Science and Technology (KIST) Institution Program (Grant nos. 2E32942, 2V09840-23-P024, and 2V09703), KU-KIST School project, the Institute of information & communications Technology Planning & Evaluation (IITP) (Grant. no.2020-0-00841), and the National Research Foundation of Korea (NRF) (Grant nos. 2023R1A2C2003985, 2021M3H4A6A02050353, and 2022M3D1A2095315). J.A. acknowledges financial support from First Research Fund Program in Life at Changwon National University in 2023. The authors thank the Pohang Accelerator Laboratory for allocating synchrotron radiation beam time (PAL 3C and 4A1, Republic of Korea).

Conflict of Interest

The authors declare no conflict of interest.

Data Availability Statement

The data that support the findings of this study are available from the corresponding author upon reasonable request.

Keywords

field-effect transistor, logic application, $MoTe_2$, reversible polarity control

Received: March 8, 2024
Revised: April 27, 2024
Published online: May 15, 2024

[1] S. Y. Seo, G. Moon, O. F. N. Okello, M. Y. Park, C. Han, S. Cha, H. Choi, H. W. Yeom, S. Y. Choi, J. Park, M. H. Jo, *Nat. Electron.* **2021**, *4*, 38.
[2] J. Jang, H. S. Ra, J. Ahn, T. W. Kim, S. H. Song, S. Park, T. Taniguch, K. Watanabe, K. Lee, D. K. Hwang, *Adv. Mater.* **2022**, *34*, 2109899.
[3] J. E. Seo, T. Das, E. Park, D. Seo, J. Y. Kwak, J. W. Chang, *ACS Appl. Mater. Interfaces* **2021**, *13*, 43480.
[4] Q. H. Wang, K. Kalantar-Zadeh, A. Kis, J. N. Coleman, M. S. Strano, *Nat. Nanotechnol.* **2012**, *7*, 699.
[5] X. Liu, A. Islam, J. Guo, P. X. L. Feng, *ACS Nano* **2020**, *14*, 1457.
[6] M. Chhowalla, H. S. Shin, G. Eda, L. J. Li, K. P. Loh, H. Zhang, *Nat. Chem.* **2013**, *5*, 263.
[7] K. F. Mak, J. Shan, *Nat. Photonics* **2016**, *10*, 216.
[8] J. Ahn, K. Ko, J. H. Kyhm, H. S. Ra, H. Bae, S. Hong, D. Y. Kim, J. Jang, T. W. Kim, S. Choi, J. H. Kang, N. Kwon, S. Park, B. K. Ju, T. C. Poon, M. C. Park, S. Im, D. K. Hwang, *ACS Nano* **2021**, *15*, 17917.
[9] L. G. Kong, X. D. Zhang, Q. Y. Tao, M. L. Zhang, W. Q. Dang, Z. W. Li, L. P. Feng, L. Liao, X. F. Duan, Y. Liu, *Nat. Commun.* **2020**, *11*, 1866.
[10] A. Eftekhari, *J. Mater. Chem. A* **2017**, *5*, 18299.
[11] S. Y. Zhang, H. M. Hill, K. Moudgil, C. A. Richter, A. R. H. Walker, S. Barlow, S. R. Marder, C. A. Hacker, S. J. Pookpanratana, *Adv. Mater.* **2018**, *30*, 1802991.
[12] J. Gao, Y. D. Kim, L. B. Liang, J. C. Idrobo, P. Chow, J. W. Tan, B. C. Li, L. Li, B. G. Sumpter, T. M. Lu, V. Meunier, J. Hone, N. Koratkar, *Adv. Mater.* **2016**, *28*, 9735.
[13] V. P. Pham, G. Y. Yeom, *Adv. Mater.* **2016**, *28*, 9024.
[14] G. Gawlik, P. Ciepielewski, J. M. Baranowski, *Appl. Sci.* **2019**, *9*, 544.
[15] P. C. Shen, C. Su, Y. X. Lin, A. S. Chou, C. C. Cheng, J. H. Park, M. H. Chiu, A. Y. Lu, H. L. Tang, M. M. Tavakoli, G. Pitner, X. Ji, Z. Y. Cai, N. N. Mao, J. T. Wang, V. C. Tung, J. Li, J. Bokor, A. Zettl, C. I. Wu, T. Palacios, L. J. Li, J. Kong, *Nature* **2021**, *593*, 211.
[16] S. Das, H. Y. Chen, A. V. Penumatcha, J. Appenzeller, *Nano Lett* **2013**, *13*, 100.
[17] R. T. Tung, *Appl. Phys. Rev.* **2014**, *1*, 011304.
[18] T. D. Ngo, Z. Yang, M. Lee, F. Ali, I. Moon, D. G. Kim, T. Taniguchi, K. Watanabe, K. Y. Lee, W. J. Yoo, *Adv. Electron. Mater.* **2021**, *7*, 2001212.
[19] Z. Yang, C. Kim, K. Y. Lee, M. Lee, S. Appalakondaiah, C. H. Ra, K. Watanabe, T. Taniguchi, K. Cho, E. Hwang, J. Hone, W. J. Yoo, *Adv. Mater.* **2019**, *31*, 1808231.
[20] Y. Liu, J. Guo, E. B. Zhu, L. Liao, S. J. Lee, M. N. Ding, I. Shakir, V. Gambin, Y. Huang, X. F. Duan, *Nature* **2018**, *557*, 696.
[21] S. Chuang, C. Battaglia, A. Azcatl, S. McDonnell, J. S. Kang, X. T. Yin, M. Tosun, R. Kapadia, H. Fang, R. M. Wallace, A. Javey, *Nano Lett.* **2014**, *14*, 1337.
[22] Y. Y. Liu, P. Stradins, S. H. Wei, *Sci. Adv.* **2016**, *2*, 1600069.
[23] D. S. Qu, X. C. Liu, M. Huang, C. Lee, F. Ahmed, H. Kim, R. S. Ruoff, J. Hone, W. J. Yoo, *Adv. Mater.* **2017**, *29*, 1606433.
[24] M. Yamamoto, S. Nakaharai, K. Ueno, K. Tsukagoshi, *Nano Lett.* **2016**, *16*, 2720.
[25] Y. J. Park, A. K. Katiyar, A. T. Hoang, J. H. Ahn, *Small* **2019**, *15*, 1901772.
[26] G. V. Resta, S. Sutar, Y. Balaji, D. Lin, P. Raghavan, I. Radu, F. Catthoor, A. Thean, P. E. Gaillardon, G. de Micheli, *Sci. Rep.* **2016**, *6*, 29448.
[27] J. Ahn, J. H. Kyhm, H. K. Kang, N. Kwon, H. K. Kim, S. Park, D. K. Hwang, *ACS Photonics* **2021**, *8*, 2650.
[28] X. J. Liu, H. Yang, J. He, H. X. Liu, L. D. Song, L. Li, J. Luo, *Small* **2018**, *14*, 1704049.
[29] H. S. Liu, N. N. Han, J. J. Zhao, *RSC Adv.* **2015**, *5*, 17572.
[30] X. C. Liu, D. S. Qu, L. Wang, M. Huang, Y. H. Yuan, P. Chen, Y. Y. Qu, J. Sun, W. J. Yoo, *Adv. Funct. Mater.* **2020**, *30*, 2004880.
[31] J. K. Liu, Y. Y. Wang, X. Y. Xiao, K. A. Zhang, N. Guo, Y. Jia, S. Y. Zhou, Y. Wu, Q. Q. Li, L. Xiao, *Nanoscale Res. Lett.* **2018**, *13*, 291.
[32] L. Yang, H. Wu, W. F. Zhang, X. Lou, Z. J. Xie, X. Yu, Y. Liu, H. X. Chang, *Adv. Electron. Mater.* **2019**, *5*, 1900552.
[33] M. S. Choi, M. Lee, T. D. Ngo, J. Hone, W. J. Yoo, *Adv. Electron. Mater.* **2021**, *7*, 2100449.
[34] Y. Guo, S. Zhou, J. J. Zhao, *ChemNanoMat* **2020**, *6*, 838.
[35] B. Chen, H. Sahin, A. Suslu, L. Ding, M. I. Bertoni, F. M. Peeters, S. Tongay, *ACS Nano* **2015**, *9*, 5326.
[36] L. Lin, Z. Y. Feng, Z. Z. Dong, C. C. Hu, L. H. Han, H. L. Tao, *Phys. E: Low-Dimens. Syst. Nanostructures* **2023**, *145*, 115489.
[37] Y. X. Ke, D. Y. Qi, C. Han, J. D. Liu, J. Q. Zhu, Y. J. Xiang, W. J. Zhang, *ACS Appl. Electron. Mater.* **2020**, *2*, 920.
[38] M. J. Mleczko, A. C. Yu, C. M. Smyth, V. Chen, Y. C. Shin, S. Chatterjee, Y. C. Tsai, Y. Nishi, R. M. Wallace, E. Pop, *Nano Lett.* **2019**, *19*, 6352.
[39] J. Y. Lim, A. Pezeshki, S. Oh, J. S. Kim, Y. T. Lee, S. Yu, D. K. Hwang, G. H. Lee, H. J. Choi, S. Im, *Adv. Mater.* **2017**, *29*, 1701798.
[40] H. Liu, A. T. Neal, M. W. Si, Y. C. Du, P. D. Ye, *IEEE Electron Device Lett.* **2014**, *35*, 795.
[41] V. Popescu, A. Zunger, *Phys. Rev. B* **2012**, *85*, 085201.